Mechanism and Machine Theory 105 (2016) 583–605

Contents lists available at ScienceDirect

Mechanism and Machine Theory

journal homepage: www.elsevier.com/locate/mechmt

A cable linkage with remote centre of motion

S. Liu[a], B. Chen[a], S. Caro[b], S. Briot[b], L. Harewood[c], C. Chen[a,*]

[a]Laboratory of Motion Generation and Automation, Room G50, 17 Alliance Lane, Monash University, Victoria 3800, Australia
[b]CNRS-IRCCyN, 1 rue de la Noë, BP 92101, Nantes Cedex 3 44321, France
[c]Suite 103, Epworth Freemasons Medical Centre, 320 Victoria Parade, East Melbourne, Victoria 3002, Australia

ARTICLE INFO

Article history:
Received 21 March 2016
Received in revised form 25 July 2016
Accepted 26 July 2016
Available online xxxx

Keywords:
Remote centre of motion
Cable system
Constraint approach
Minimally-invasive surgery

ABSTRACT

Mechanical remote centre of motion (RCM) mechanisms are often used to construct robotic minimally-invasive surgical manipulators, such that potential damage on the incision ports is eliminated. Current parallelogram-based RCM linkages (PB-linkage) typically have large footprints that compromise optimal surgical operations. A novel cable system with remote centre of motion is proposed to reduce the footprint. The RCM function of the cable system is proven mathematically. A new approach based on constraint analysis is conducted to determine the magnitudes of tension. The results are validated by finite element analysis, hence proves the use of constraint approach and the functioning of the cable system. Upon verification, the footprint of the cable linkage is compared to that of a PB-linkage in a simplified surgical scenario through three approaches. The quantitative analysis shows that the cable linkage has a smaller footprint in more than half of the design points in all approaches. A prototype is built for proofing the concept of the cable linkage.

1. Introduction

In a minimally-invasive surgery (MIS), the surgical instrument is constrained to have four degrees-of-freedom (DOF) through the incision port [1]: pitch, yaw, translation along the longitudinal axis and roll. The first three DOF in combine function as a spherical coordinate system to define the position of end-effector inside the patient's body. Remote centre of motion (RCM) mechanisms provide the two rotational DOF while permitting the surgical instrument to pivot around the incision port, hence eliminate potential damage to the incision port and promote the safety of MIS procedures [2].The RCM function refers to the capability of a mechanism to rotate its link(s) around a remote point without having a physical revolute joint at the point [3,4]. A remote centre (RC) can be constrained virtually or mechanically [5]. Mechanical RCM mechanisms are more reliable and considered suitable for clinical applications [3]. Mechanical RCM mechanisms that generate single RC and are applied on robotic MIS systems include isocentres [6], circular tracking arcs [7,8], parallelograms [9–14], synchronous transmissions [15] and spherical linkages [16]. In addition, there are RCM mechanisms that generate multiple RCs [17].

A commonly used approach to synthetise a two-DOF RCM mechanism is to combine a planar RCM mechanism with a revolute joint [3]. The axis of the revolute joint coincides with the one-DOF RC to add the second DOF. Such approach results in fully

* Corresponding author.
E-mail addresses: shao.liu@monash.edu (S. Liu), binbin.chen@monash.edu (B. Chen), stephane.caro@irccyn.ec-nantes.fr (S. Caro), sebastien.briot@irccyn.ec-nantes.fr (S. Briot), laurenceharewood@urologyvictoria.com (L. Harewood), chao.chen@monash.edu (C. Chen).

http://dx.doi.org/10.1016/j.mechmachtheory.2016.07.023
0094-114X/

decoupled rotational DOF, whose benefits include reduced complexity in control, promoted level of confidence in safety as well as rapid and intuitive manual positioning of the entire mechanism or individual DOF [1].

The translational DOF required in the MIS applications is often achieved by mounting an independent translational mechanism on the two-DOF RCM mechanism. A typical example of such three-DOF mechanism is the clinically-approved da Vinci series robotic surgical system [11,18,19]. In other approaches, various types of RCM mechanisms that also provide translational DOF are explored [20–22]. However, these mechanisms have coupled DOF [20], or are relatively bulky in terms of the transverse dimension [21], or have large sweeping volume upon rotation of the planar RCM mechanism around the revolute joint, due to the large enclosed area by the outer boundary of the planar RCM mechanism [22].

The parallelogram-based structure is widely used as the planar RCM mechanism in the robotic MIS systems [3]. However, there are footprint issues associated with the parallelogram-base linkages (PB-linkage), which the consequences being poor access for bedside assistance [19] and the compromise in optimal surgical functioning [23]. The term "footprint" is mostly referred to as the sweeping volume of the RCM mechanism, which is generated by the rotation of the planar RCM mechanism around the revolute joint. The sweeping volume is thus related to the area enclosed by the outer boundary of the planar RCM mechanism.

When the output link of the parallelogram is short, the output joint of the PB-linkage is positioned closely to the incision ports. Given that the space around an incision port is often crowded with robotic or manual surgical tools, the collision-free workspace is reduced and the chance of interference is increased. The transmission for the translational mechanism mounted on the output link of the PB-linkage goes through the output joint, causing further expansion in size.

In opposite case where a longer output link is used to displace the output joint away from the mechanism, the size of the parallelogram and thus the enclosed area is increased. The consequence being the increase in the sweeping volume, which again leads to increase in chance of interference. Apart from the sweeping volume, longer links occupy more space even when the linkage is stationary. It also increases the weight and inertia of the system. Quantitative analysis on the footprint of the PB-linkage though three approaches is presented in Section 5.

This paper proposes a cable linkage with RCM, in the attempt to address the footprint issue associated with the PB-linkage. The entire RCM mechanism is kept relatively faraway from the RC, when the distance between the input joint and the RC is given. A cantilever is rigidly mounted on to the output link. It is the only part of the entire RCM mechanism that is operated near the RC. Therefore, the cable system can leave more collision-free workspace for the neighbouring robotic surgical arms or human surgeons to operate. In addition, the enclosed area of the planar RCM is relatively small, resulting in a smaller sweeping volume. Further, the links are relatively short, which reduces the space taken by the links when stationary, and potentially reduce the weight and inertia of the mechanism. A comparison between footprint of the proposed linkage and the PB-linkage is presented in Section 5.

Cable-pulley mechanism provides advantages such as structure simplicity, compactness, light weight, low friction and low backlash [24]. Therefore it is widely applied on serial and parallel robotic manipulators, as summarised in [25] and [26], respectively. In MIS applications, the evolution from linkage-based da Vinci system [11] to cable-based da Vinci systems [18,19] shows significant deduction in the size of linkage. As such, the proposed planar RCM mechanism is developed based on cable-pulley mechanism.

Cable tension analysis is essential for proof of functioning of the cable linkage. Approaches for describing cable tension of cable-constrained open-chain linkage and multi-link parallel manipulator are available in [27] and [28], respectively. However, a more generalised approach based on mechanical constraint [29] is used in the analysis. The reason being that the proposed linkage is based on four-bar linkage and is affected by the singularity of an unconstrained four-bar linkage. The constraint approach provides indication on the constraint status of the mechanism, thus enable justification on the removal of singularity. The cable tension is solved as generalised force along mechanical constraints. Numerical solution of cable tension is obtained using QR decomposition and verified with static finite element simulation in ANSYS.

The rest of the paper is arranged as follows. Section 2 describes the design of the cable linkage and the proof of the RCM function. Section 3 applies the constraint-based analysis. Constraint equations are derived. Cable tension is solved and verified with finite element analysis. The functioning of the cable loops is hence proven. Section 4 calculates the minimum required cable stiffness to achieve a given overall stiffness of the linkage. Section 5 compares the footprints of the cable linkage and PB-linkage in a simplified surgical scenario. Section 6 introduces the prototype of the cable linkage.

2. The cable linkage with RCM

In this section, the design of cable linkage with RCM is presented, along with the proof of RCM under the condition that the cable is in tension.

2.1. Design of cable linkage

The design of the cable linkage with RCM is illustrated in Figs. 1 and 2, where the schematic diagram of links (without cable loops) and the full schematic diagram are presented, respectively. The cable linkage consists of eight links and seven pulleys that are arranged in three cable loops. As illustrated in Fig. 1, the links are AF, AC, CE, EH, BG, DG, CI and IG, respectively. Joint I is a passive prismatic joint while all other joints (indicated by the small circles) are revolute joints. Note that joints B and D do not divide links AC and CE, respectively. For convenience, links CI, IG and passive prismatic joint I are grouped and termed "diagonal link CG" in the later descriptions. Different configurations of the cable linkage are presented in Figs. 3 and 4. ROM in

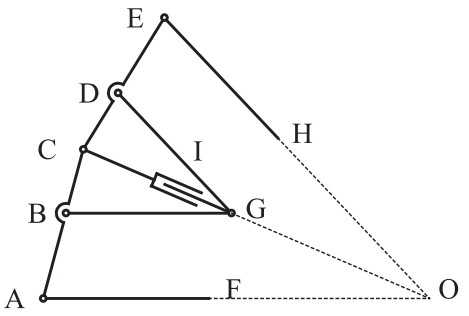

Fig. 1. Configuration of links.

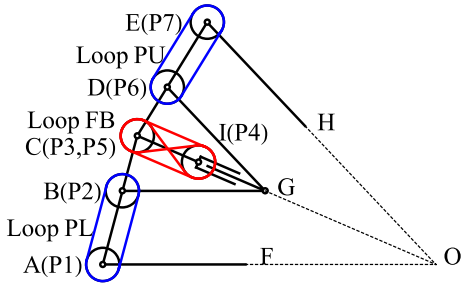

Fig. 2. Configuration of links and cable loops.

the figures stands for range of motion. The limits in ROM above and below the ground (AO), and the centre configuration where all links are overlapped with the ground are illustrated in Fig. 3. Two mid-point configurations in between the centre and two limits in ROM are illustrated in Fig. 4. Note that pulleys and cable loops are not drawn for clarity of figures. In Fig. 3, all labelled joints are for the centre configuration only, where all the links overlap with the ground while D, E and H are coincident with B, A and F, respectively.

Point O is the remote centre. Links AF, AC, CE and EH are the ground, input, connector and output links, respectively. Links AC and CE, with virtual links AO and EO, form virtual four-bar linkage ACEO. Links BG and DG constraint the motion of the linkage. Link CG is the diagonal link of the virtual four-bar linkage. It contains a passive prismatic joint, Joint I, to accommodate for the change in length of CG with respect to movement of linkage. The distance between Joints C and I is constant while the distance between Joints I and G changes. The shape and size of output Link EH can be optimised freely to suit specific MIS applications.

The three cable loops are called Loops PL, FB and PU, for the lower, middle and upper loops in Fig. 2, respectively. Loop PL connects Pulleys P1 and P2, which are rigidly attached to Links AF and BG, respectively. Loop FB connects Pulleys P3 to P5. Pulley P3 is rigidly attached to Link AC. Pulley P4 rotates freely at I. Pulley P5 is rigidly attached to Link CE. The cable connecting P4 and

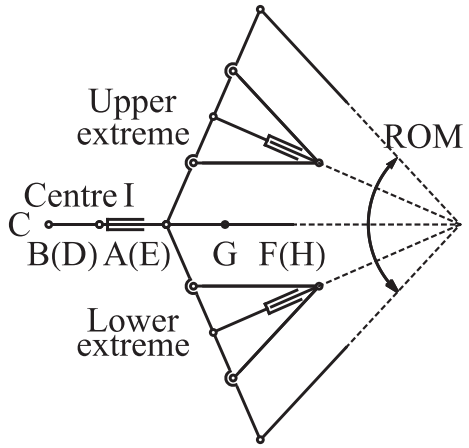

Fig. 3. Configurations at two extremes and centre of ROM.

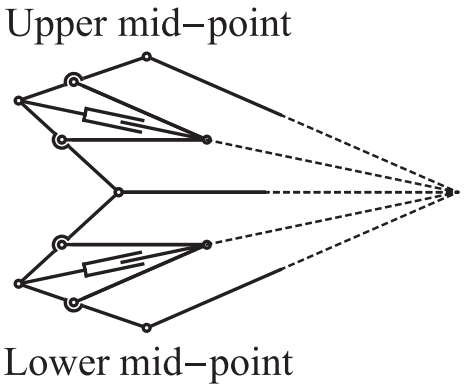

Fig. 4. Configurations at mid-points.

P5 has crossed configuration. Loop PU connects Pulleys P6 and P7, which are rigidly attached to Links DG and EH, respectively. Note that although there exist two forms of cable loop, which are the end-less tendon drive and the open-ended tendon drive, as classified in [25], they are not distinguished in the 2D design of the cable linkage. The reason is that the synchronised rotation of pulleys, which is the essential mechanical constraint of the cable linkage, can be achieved equivalently using two forms of cable loop under the assumptions of zero cable slippage elongation.

Loops PL and PU ensure Links BG and EH are parallel to AF and DG, respectively. Slip of cable on pulleys in Loops PL and PU ruins the parallel constraint, thus cause failure in maintaining the RCM function. Loop FB permits the cable linkage to pass the configuration where all links overlap with the ground, which is the singular configuration of an unconstrained four-bar linkage. Slip of cable in Loop FB does not affect the RCM function. In non-overlapped configurations, Loop FB is redundant. In the overlap configuration, slip of cable in Loop FB can cause the cable linkage to turn into an undesired configuration, where the output link stays coincident with the ground regardless of the input angle. Thus the position of the remote centre is not affected, despite the lost of mobility. More details regarding the singularity are described in the later paragraphs of this section.

The outer shape of the cable linkage, which is virtual four-bar linkage ACEO, is symmetrical to simplify the geometry. Links AC and CE have equal link length. Virtual links AO and CO have another equal link length, which is longer than that of AC and CE. Such structure ensures that the link length of the RCM mechanism is always smaller than the distance between the input joint A and the remote centre O. Hence the RCM mechanism is considered to be relatively faraway from the remote centre.

The geometry of the linkage is fully defined by two parameters, v and r, expressed mathematically as

$$v = \frac{L_{AC}}{L_{AO}} = \frac{L_{CE}}{L_{EO}} \tag{1}$$

and

$$r = \frac{L_{AC}}{L_{AB}} = \frac{L_{CE}}{L_{DE}} \tag{2}$$

To ensure Links AC and CE are shorter than AO and CO, v is smaller than one. With a given length AO, the range of motion (ROM) of the RCM mechanism is fully defined by v. As shown in Fig. 3, the centre (diagonal) line CO is perpendicular to ACE at two ends of ROM. Therefore, the ROM is

$$ROM = 4 \arcsin v \tag{3}$$

Parameter r is greater than one. It defines the geometry of four-bar linkage BCDG, where the length of Links BG and DG is

$$L_{BG} = L_{DG} = \left(1 - \frac{1}{r}\right) L_{AO} \tag{4}$$

Eq. (4) indicates that the larger the r, the longer Links BG and DG are. Four-bar linkage BCDG occupies additional space between Links AC, CE and the RC, thus a smaller r is desired to leave more clearance around the RC.

The configuration where all links overlap with ground is a bifurcation (singularity) configuration of an unconstrained four-bar linkage, where two possible configurations can be achieved upon crossing

$$\angle BCD = \angle BGD = 0 \tag{5}$$

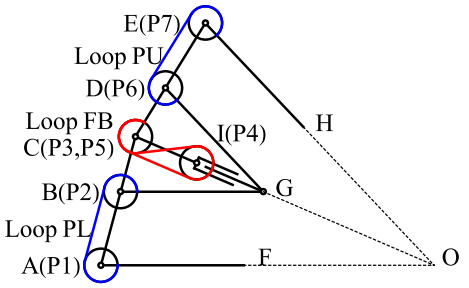

Fig. 5. Cables in tension in upward motion.

and

$$\angle BCD = 2\angle BCG \tag{6}$$

where Eq. (6) can be equivalently expressed as

$$\angle BGD = 2\angle BGC \tag{7}$$

The first configuration shown in Eq. (5) is an undesired configuration where Links BG, DG and EH stay overlapped with ground (AF/AO) regardless of the input angle. In this case the mobility of the linkage is lost. Therefore, Eq. (6) or (7) needs to be enforced to fully constrain the linkage.

The cable linage achieves Eq. (6). In Loop FB, $\angle BCG$ and $\angle DCG$ are related to the relative rotations of Pulleys P3 and P5 with respect to diagonal link CG, respectively. Pulley P4 allows the two angles to be synchronised hence eliminates the chance of turning into Eq. (5). In this design, P3 and P5 are placed at Joint C to maximise the clearance between Links AC, CE and the RC.

The cable on one side of a loop is in tension in one direction of motion of the linkage. The sides of loops that are in tension in the upward and downward motions of the linkage are shown in Figs. 5 and 6, respectively.

2.2. Proof of RCM function

The proof of RCM function of the cable linkage is conducted based on the condition that the cable loops are functioning correctly hence the linkage is in the desired configuration. Such condition is proven in the Section 3. Given that an RCM mechanism requires a link to rotate around the remote centre, the proof is conducted through two steps:

1. Joint E rotates around O with a constant radius.
2. Point H rotates around O with a constant radius.

where E and H form output link EH.
To simplify the expressions, the following link lengths are assigned.

$$\begin{aligned} L_1 &= L_{AC} = L_{CE} = vL_{AO} \\ L_2 &= L_{AB} = L_{DE} = \frac{L_{AC}}{r} = \frac{vL_{AO}}{r} \\ L_3 &= L_{AF} = L_{BG} = L_{DG} = L_{EH} = \left(1 - \frac{1}{r}\right) L_{AO} \end{aligned} \tag{8}$$

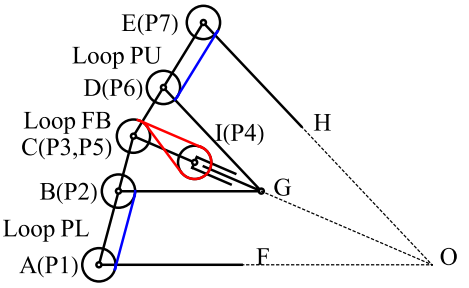

Fig. 6. Cables in tension in downward motion.

Table 1
List of generalised coordinates.

q	Definition	Reference
θ_1	Angle of Link AC	$\vec{AF}$
θ_2	Angle of Link BG and P2	$\vec{AC}$
θ_4	Angle of P4	$\vec{CG}$
θ_6	Angle of Link DG and P6	$\vec{CE}$
θ_7	Angle of Link EH and P7	$\vec{CE}$
θ_8	Angle of Link CG	$\vec{AC}$
θ_9	Angle of Link CE	$\vec{GC}$
L_{CG}	Distance between CG	n/a
x_H	Horizontal position of H	A
y_H	Vertical position of H	A

2.2.1. Generalised coordinates

To conduct the proof, ten generalised coordinates are assigned to fully describe the linkage. The generalised coordinates q are listed in Table 1.

θ_1 is the actuator input angle thus it is the independent generalised coordinate. All other generalised coordinates are dependent ones. The angles are measured with respect to the "previous" link, as shown in the "Reference", and in counter-clockwise (CCW) direction. There is no θ_3 and θ_5 since Pulleys P3 and P5 are rigidly attached to links and do not have their own independent rotation. The graphical representation of the generalised coordinates is shown in Fig. 7.

2.2.2. Step 1 - position of joint E

The distance between Joint E and O is

$$L_{EO} = \sqrt{(x_E - L_{AO})^2 + y_E^2} \tag{9}$$

where x_E and y_E are the horizontal and vertical positions of Joint E with respect to Joint A, respectively

$$\begin{aligned} x_E &= L_1 \cos\theta_1 + L_1 \cos(\theta_1 + \theta_8 + \pi + \theta_9) \\ y_E &= L_1 \sin\theta_1 + L_1 \sin(\theta_1 + \theta_8 + \pi + \theta_9) \end{aligned} \tag{10}$$

where the π term is added as θ_9 is measured with respect to $\vec{GC}$ instead of $\vec{CG}$. The objective of Step 1 is to prove that L_{EO} is a constant. θ_8 and θ_9 need to be eliminated when Eq. (10)is substituted into Eq. (9).

θ_8 is calculated by subtracting the angle of Links AC with respect to ground from the angle of Link CG with respect to ground, i.e.

$$\theta_8 = \angle\vec{CG} - \angle\vec{AC} \tag{11}$$

Since Loop PL ensures that triangles BCG and ACO are similar triangles, the angle of Link CG with respect to ground is the same as the angle of diagonal line CO with respect to ground

$$\angle\vec{CG} = \angle\vec{CO} = -\arctan\frac{L_1 \sin\theta_1}{L_{AO} - L_1 \cos\theta_1} \tag{12}$$

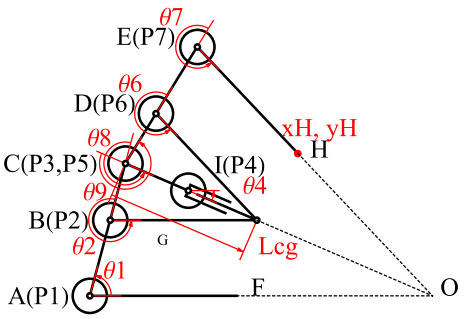

Fig. 7. Generalised coordinates.

The angle of Link AC with respect to ground is simply θ_1, thus

$$\theta_8 = \angle\vec{CG} - \angle\vec{AC} = -\arctan\frac{L_1\sin\theta_1}{L_{AO} - L_1\cos\theta_1} - \theta_1 \tag{13}$$

Due to the symmetrical structure of four-bar linkage BCDG

$$\theta_9 = \theta_8 = -\arctan\frac{L_1\sin\theta_1}{L_{AO} - L_1\cos\theta_1} - \theta_1 \tag{14}$$

Substituting Eqs. (10), (13) and (14) into Eq. (9) yields

$$L_{EO} = L_{AO} \tag{15}$$

Hence Joint E is proven to rotate around O.

2.2.3. Step 2 - position of point H

The position of Point H is determined through a similar approach as that of Joint E. The distance between Point H and O is

$$L_{HO} = \sqrt{(xH - L_{AO})^2 + y_H^2} \tag{16}$$

where x_H and y_H are

$$\begin{aligned} x_H &= L_1\cos\theta_1 + L_1\cos(\theta_1 + \theta_8 + \pi + \theta_9) + L_3\cos(\theta_1 + \theta_8 + \pi + \theta_9 + \theta_7) \\ y_H &= L_1\sin\theta_1 + L_1\sin(\theta_1 + \theta_8 + \pi + \theta_9) + L_3\sin(\theta_1 + \theta_8 + \pi + \theta_9 + \theta_7) \end{aligned} \tag{17}$$

Given cable loop PU, the angles of Links EH and DG with respect to the ground are equal. Therefore, θ_7 and θ_6 are equal. From Eq. (7), the angle of Link DG with respect to ground is given by

$$\angle\vec{DG} = 2\angle\vec{CG} = -2\arctan\frac{L_1\sin\theta_1}{L_{AO} - L_1\cos\theta_1} \tag{18}$$

Hence

$$\theta_7 = \theta_6 = \angle\vec{DG} - \angle\vec{CE} = -2\arctan\frac{L_1\sin\theta_1}{L_{AO} - L_1\cos\theta_1} - (\theta_1 + \theta_8 + \pi + \theta_9) = \theta_1 - \pi \tag{19}$$

Substituting Eqs. (12), (13), (17) and (19) into Eq. (16) yields

$$L_{HO} = \frac{L_{AO}}{r} \tag{20}$$

Therefore L_{HO} is a constant. Since both L_{EO} and L_{HO} are constant, Link EH is proven to rotate around the remote centre and the cable linkage is proven to be an RCM mechanism.

3. Cable tension analysis

The RCM function proven in Section 2 is conducted under the condition that the cable loops are functioning. To achieve such condition, the following criteria must be achieved:

1. The cable loops (especially Loop FB) must not obstruct the movement of the links.
2. The two sides of a cable loop must be in tension in each direction of motion of the linkage, respectively.

The functioning of cable linkage is proven through constraint approach analysis. Criterion 1 is proven based on the constraint equations derived from cable loops. Criteria 2 is proven based on the solutions of cable tension. In addition, the cable linkage is also proven to be fully-constrained (singularity-free) based on the number of constraint equations derived. The full proof is presented in this section.

3.1. The constraint approach

Such constraint-based analysis is based on a generalised constraint approach [29], which is briefed below.

The dynamics of a constrained physical system is described as [30]

$$Q_i = Q_c + Q_e \tag{21}$$

where Q_i, Q_c and Q_e are the generalised inertia, constraint and external forces applied on the generalised coordinates q, respectively. The generalised constraint force Q_c applied on q is related to the mechanical constraints of the systems through

$$Q_c = -C_q^T \lambda \tag{22}$$

where λ is the Lagrange multiplier, which represents the generalised constraint force acting along the mechanical constraints. C_q is the derivative of the constraint matrix c_q with respect to the generalised coordinates q, which is

$$C_q = \frac{\partial c_q}{\partial q} \tag{23}$$

c_q represents the mechanical constraints of the system. Assuming that c_q and q have dimensions of m and n respectively, the dimensions of Q_c, C_q and λ are $n \times 1$, $m \times n$, and $m \times 1$, respectively. The cable linkage (one-DOF) is fully constrained when n equals $(m + 1)$. In the cable linkage, the constraints from cable loops are contained in c_q. Hence, c_q can be used to prove Criterion 1.

C_q and c_q also satisfy

$$\frac{\partial c}{\partial q_d}\dot{q_d} + \frac{\partial c}{\partial q_i}\dot{q_i} = C_{qd}\dot{q_d} + C_{qi}\dot{q_i} = 0 \tag{24}$$

where q_i and q_d are the independent and dependent generalised coordinates, respectively. C_{qi} and C_{qd} are the derivative matrices determined using q_i and q_d, respectively.

In static analysis, the generalised inertia force Q_i vanishes. Therefore, combining Eqs. (21) and (22) gives

$$Q_e = C_q^T \lambda \tag{25}$$

or equivalently

$$\begin{aligned} Q_{ei} &= C_{qi}^T \lambda \\ Q_{ed} &= C_{qd}^T \lambda \end{aligned} \tag{26}$$

where Q_{ei} and Q_{ed} are the generalised external forces applied on q_i and q_d, respectively.

Eq. (25) or (26) is used to determine the generalised constraint force λ acting along the mechanical constraints, when external load Q_e is given. Cable tension is contained in λ and thus proves Criterion 2. One constraint equation for each pair of pulleys needs be derived to determine the cable tension, for each direction of motion of the linkage.

The direction of such constraint force is dependent on the way in which the constraint equation c_q is written in. An example is given below. Consider an arbitrary constraint equation that is defined as

$$c_q = p_a - p_b \tag{27}$$

where p_a and p_b are the physical quantities of Bodies A and B, respectively, which are used to construct the constraint equation. In this case the λ determined using such constraint equation is the generalised constraint force acting on Body B by Body A. In the opposite case, if the positions of p_a and p_b are swapped in Eq. (27), λ will give the generalised constraint force acting on Body A by Body B.

3.2. Analysis on cable loops

In this analysis, it is assumed that the cable is inextensible and there is no slip between the cable and pulleys. All the bodies are assumed to be rigid bodies with zero mass.

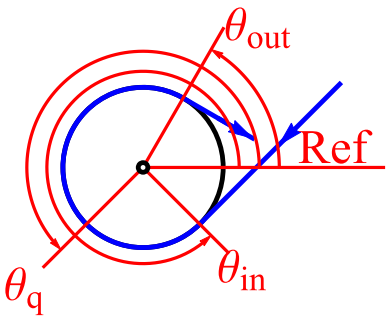

Fig. 8. Clockwise cable wrapping.

3.2.1. Constraint equations from cable loops

Given constant length of cable section connecting two pulleys and constant distance between pulleys, the sum of lengths of cable sections wrapping on two pulleys is also a constant. This is expressed mathematically as

$$L_{PA} + L_{PB} = L_{const.} \tag{28}$$

where L_{PA} and L_{PB} are the lengths of cable sections wrapping on arbitrary driving pulley PA and driven pulley PB. $L_{const.}$ is a constant that contains the overall length of cable section and the distance between two pulleys. Since the lengths of cable wrapping on pulleys are related to the rotation of pulleys and their adjacent links, generalised coordinates are embedded in Eq. (28).

Rearranging Eq. (28) into the form of Eq. (27) yields

$$(L_{const.} - L_{PB}) - L_{PA} = 0 \tag{29}$$

thus according to the definition of Eq. (27), Eq. (29) gives the force applied by the cable section attached to Pulley PB on that attached to PA.

Since the cable can wrap on a pulley in either clockwise or counter-clockwise direction, the expressions for L_{PA} and L_{PB} need to take into account the direction. The cases corresponding to clockwise and counter-clockwise cable wrapping are illustrated in Figs. 8 and 9, respectively.

In Figs. 8 and 9, "Ref" represents an arbitrary reference where the angles are measured with respect to. θ_{in}, θ_q and θ_{out} are the angle where the cable starts to wrap on the pulley, generalised coordinate and angle where cable leaves the pulley, respectively.

In the clockwise case, θ_{in} is the largest angle, followed by θ_q and θ_{out}. The length of cable from θ_{in} to θ_q is

$$L'_{CW} = R\,(\theta_{in} - \theta_q) \tag{30}$$

and the length of cable from θ_q to θ_{out} is

$$L''_{CW} = R\,(\theta_q - \theta_{out}) \tag{31}$$

In the counter-clockwise case, θ_{out} is the largest angle, followed by θ_q and θ_{in}. The length of cable from θ_{in} to θ_q is

$$L'_{CCW} = R\,(\theta_q - \theta_{in}) \tag{32}$$

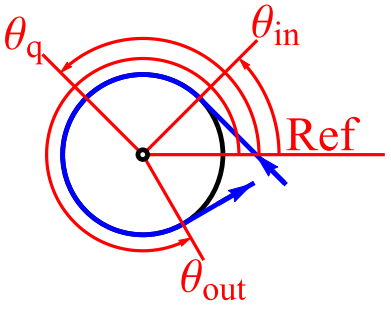

Fig. 9. Counter-clockwise cable wrapping.

Table 2
Cable and pulley angles for upward motion.

Pulley	θ_{in} (rad)	θ_q (rad)	θ_{out} (rad)	Direction	Reference
P1	n/a	0	$\theta_1 + \pi/2$	CW	$\vec{AF}$
P2	$\pi/2$	θ_2	n/a	CW	$\vec{AC}$
P3	n/a	0	$\theta_8 - \pi/2$	CCW	$\vec{AC}$
P4	$-\pi/2$	θ_4	$\pi/2 + \phi$	CCW	$\vec{CG}$
P5	$\pi/2 + \phi$	θ_9	n/a	CW	$\vec{GC}$
P6	n/a	θ_6	$\pi/2$	CW	$\vec{CE}$
P7	$\pi/2$	θ_7	n/a	CW	$\vec{CE}$

Table 3
Cable and pulley angles for downward motion.

Pulley	θ_{in} (rad)	θ_q (rad)	θ_{out} (rad)	Direction	Reference
P1	n/a	0	$\theta_1 - \pi/2$	CCW	$\vec{AF}$
P2	$-\pi/2$	θ_2	n/a	CCW	$\vec{AC}$
P3	n/a	0	$\theta_8 + \pi/2$	CW	$\vec{AC}$
P4	$\pi/2$	θ_4	$-\pi/2 - \phi$	CW	$\vec{CG}$
P5	$-\pi/2 - \phi$	θ_9	n/a	CCW	$\vec{GC}$
P6	n/a	θ_6	$-\pi/2$	CCW	$\vec{CE}$
P7	$-\pi/2$	θ_7	n/a	CCW	$\vec{CE}$

Table 4
Joints for constraint equations.

Joint	Path 1	Path 2
G	AB-BG	AC-CG
G	AB-BG	AC-CD-DG
H	x_H and y_H	AC-CE-EH

and the length of cable from θ_q to θ_{out} is

$$L''_{CCW} = R\,(\theta_{out} - \theta_q) \tag{33}$$

The θ_{in}, θ_q and θ_{out} for all the pulleys are summarised in Tables 2 and 3. Tables 2 and 3 correspond to the cable sections for upward and downward motions of the cable linkage, respectively, as illustrated in Figs. 5 and 6, respectively. ϕ is the additional constant angle introduced by crossed cable between P4 and P5. CW and CCW indicate clockwise and counter-clockwise directions, respectively. Substituting the θ terms from Tables 2 and 3 into Eq. (28) yields four constraint equations for each of the upward and downward motions of the cable linkage, respectively, which are between P1 and P2, P3 and P4, P4 and P5, and P6 and P7, respectively.

3.2.2. Constraint equation from joint positions

Apart from the cable loops, there are constraint equations from joint positions. Such constraint equations are derived based on shared joint position of two links. For example, position of Joint G can be derived from two paths: Links AB-BG and Links AC-CG, respectively. The position derived from the two paths must be identical

$$\begin{aligned} x_{G|BG} - x_{G|CG} &= 0 \\ y_{G|BG} - y_{G|CG} &= 0 \end{aligned} \tag{34}$$

where $x_{G|BG}$ and $y_{G|BG}$ are the positions derived from Links AB-BG, and $x_{G|CG}$ and $y_{G|CG}$ are the positions derived from Links AC-CG.

Six constraint equations are obtained, the paths are summarised in Table 4. Note that for Point H, the positions derived from path AC-CE-EH are equated to the generalised coordinates x_H and y_H.

3.3. Proof of Criterion 1

Criterion 1 states that with given cable length, the rotation of pulleys must be consistent with the rotation of the links they are attached to, otherwise it will jam the linkage. It can be readily seen that Criterion 1 is met in Loops PL and PU. The proof for Loop FB based on constraint approach is presented below.

The aim is to prove that the output rotation of the cable loop (θ_9) is consistent with the θ_9 derived from the links, as shown in Eq. (13), when a constant cable length from P3 to P5 is given.

Substituting the θ for P3 to P5 from Table 2 into Eq. (28) yields two constraint equations

$$R\left(\theta_4 - \left(-\frac{\pi}{2}\right)\right) + R\left(\left(\theta_8 - \frac{\pi}{2}\right) - 0\right) = L_{const.34} \tag{35}$$

for P3 and P4, and

$$R\left(\left(\frac{\pi}{2} + \phi\right) - \theta_9\right) + R\left(\left(\frac{\pi}{2} + \phi\right) - \theta_4\right) = L_{const.45} \tag{36}$$

for P4 and P5, where $L_{const.34}$ and $L_{const.45}$ are constant.

Summing Eqs. (35) and (36) gives

$$R\left(\pi + \theta_8 - \theta_9 + 2\phi\right) = L_{const.34} + L_{const.45} \tag{37}$$

Eq. (37) indicates that when given the correct cable length between P3 and P5 to start with, θ_9 equals θ_8 within full ROM of the cable linkage. Such outcome is consistent with Eq. (13), which means that the rotation of P5 is consistent with that of Link CE, thus Loop FB is not obstructing the movement of the linkage.

3.4. Constraint matrix c_q and derivative matrix C_q

Assembling the constraint equations derived from cable loops and joint positions yields the constraint matrices c_q. Individual constraint equations within the matrix are arranged in the following order

1. c_{qP12} for Pulleys P1 and P2 in Loop PL.
2. c_{qP34} for Pulleys P3 and P4 in Loop FB.
3. c_{qP45} for Pulleys P4 and P5 in Loop FB.
4. c_{qP67} for Pulleys P6 and P7 in Loop PU.
5. $c_{qGx|CG}$ for x position of Joint G from paths AB-BG and AC-CG.
6. $c_{qGy|CG}$ for y position of Joint G from paths AB-BG and AC-CG.
7. $c_{qGx|DG}$ for x position of Joint G from paths AB-BG and AC-CD-DG.
8. $c_{qGy|DG}$ for y position of Joint G from paths AB-BG and AC-CD-DG.
9. $c_{qHx|EH}$ for x position of Point H from generalised coordinate x_H and path AC-CE-EH.
10. $c_{qHy|EH}$ for y position of Point H from generalised coordinate y_H and path AC-CE-EH.

The constraint matrices are

$$c_{q1} = \begin{bmatrix} -R\left(\theta_1 + \theta_2\right) \\ R\left(\theta_4 + \theta_8\right) \\ R\left(\pi - \theta_4 - \theta_9 + 2\phi\right) \\ R\left(\theta_6 - \theta_7\right) \\ \left(L_1 - L_2\right)\cos\theta_1 - L_3\cos\left(\theta_1 + \theta_2\right) + L_{CG}\cos\left(\theta_1 + \theta_8\right) \\ \left(L_1 - L_2\right)\sin\theta_1 - L_3\sin\left(\theta_1 + \theta_2\right) + L_{CG}\sin\left(\theta_1 + \theta_8\right) \\ \left(L_1 - L_2\right)\left(\cos\theta_1 - \cos\left(\theta_1 + \theta_8 + \theta_9\right)\right) - L_3\left(\cos\left(\theta_1 + \theta_2\right) + \cos(\theta_1 + \theta_8 + \theta_9 + \theta_6)\right) \\ \left(L_1 - L_2\right)\left(\sin\theta_1 - \sin\left(\theta_1 + \theta_8 + \theta_9\right)\right) - L_3\left(\sin\left(\theta_1 + \theta_2\right) + \sin\left(\theta_1 + \theta_8 + \theta_9 + \theta_6\right)\right) \\ x_H - L_1\cos\theta_1 + L_1\cos\left(\theta_1 + \theta_8 + \theta_0\right) + L_3\cos\left(\theta_1 + \theta_8 + \theta_9 + \theta_7\right) \\ y_H - L_1\sin\theta_1 + L_1\sin\left(\theta_1 + \theta_8 + \theta_0\right) + L_3\sin\left(\theta_1 + \theta_8 + \theta_9 + \theta_7\right) \end{bmatrix} \tag{38}$$

for the upward motion of cable linkage. Note that for the constraint equations derived from cable loops, the constants associated with cable lengths are not included, as they do not appear in the derivative matrix C_q. For downward motion of the cable linkage, the joint constraint equations (last six) are the same. The cable constraint equations (first four) have negative signs to those in Eq. (38).

The derivative matrix C_q is given by

$$C_q = \begin{bmatrix} \frac{\partial c_q}{\partial \theta_1} & \frac{\partial c_q}{\partial \theta_2} & \cdots & \frac{\partial c_q}{\partial \theta_6} & \frac{\partial c_q}{\partial \theta_7} & \frac{\partial c_q}{\partial L_{CG}} & \frac{\partial c_q}{\partial x_H} & \frac{\partial c_q}{\partial y_H} \end{bmatrix} \tag{39}$$

where each column in the matrix contains the derivative of constraint matrix c_q with respect to one of the generalised coordinates. The derivative matrices C_{qi} and C_{qd} for independent and dependent generalised coordinates, respectively, are

$$C_{qi} = \begin{bmatrix} \frac{\partial c_q}{\partial \theta_1} \end{bmatrix} \tag{40}$$

and

$$C_{qd} = \left[\begin{array}{cccccc} \frac{\partial c_q}{\partial \theta_2} & \cdots & \frac{\partial c_q}{\partial \theta_6} & \frac{\partial c_q}{\partial \theta_7} & \frac{\partial c_q}{\partial L_{CG}} & \frac{\partial c_q}{\partial x_H} & \frac{\partial c_q}{\partial y_H} \end{array} \right] \tag{41}$$

which the two matrices are used for Eq. (26).

3.5. Constraint status of cable linkage

With ten generalised coordinates and ten constraint equations, the cable linkage seems to be over-constrained. However, certain retain constraint equations are redundant or vanish, resulting in fully-constrained one-DOF RCM mechanism. The cases where the links in non-overlapped and overlapped configurations are analysed separately.

In non-overlapped configurations, Loop FB is redundant. Loop FB introduces one generalised coordinate θ_4 and two constraint equations c_{qP34} and c_{qP45}. By excluding the generalised coordinate and constraint equations, the cable system is described by nine generalised coordinates with eight constraint equations. The cable linkage is fully constrained and has one DOF.

The overlapped configuration is the singular configuration of a four-bar linkage, thus $c_{qGx|DG}$ from four-bar linkage BCDG vanishes, resulting in fully-constrained cable linkage. According to the constraint approach, the elimination of $c_{qGx|DG}$ can be proven mathematically by observing zeros for its corresponding terms in C_q.

Writing θ_6 to θ_9, and L_{CG} in terms of θ_1, and substitute into C_q yields

$$\frac{\partial}{\partial q} c_{qGx|DG} = [\, 0 \;\; 0 \;\; 0 \;\; 0 \;\; 0 \;\; 0 \;\; 0 \;\; 0 \;\; 0 \;\; 0 \,] \tag{42}$$

where θ_6 to θ_9 are given by Eqs. (13), (14)and (19), respectively, and

$$L_{CG} = \left(1 - \frac{1}{r}\right) \sqrt{(L_{AO} - L_1 \cos\theta_1)^2 + (L_1 \sin\theta_1)^2} \tag{43}$$

Thus the cable linkage is described by ten generalised coordinates with night constraint equations. The cable linkage is fully constrained and has one DOF.

3.6. Calculation of cable tension

In the analysis, no external load is applied on Pulleys P2 to P6 and the passive prismatic joint I. Further, the upward and downward are simulated by applying vertical force F_{Hy} at point H. The torque on Joint E (τ_7) and horizontal force on Point H (F_{Hx}) are zero. The generalised external force Q_e applied on the generalised coordinates is given by

$$\begin{aligned} Q_e &= [\, \tau_1 \;\; \tau_2 \;\; \cdots \;\; \tau_6 \;\; \tau_7 \;\; F_{CG} \;\; F_{Hx} \;\; F_{Hy} \,] \\ &= [\, \tau_1 \;\; 0 \;\; \cdots \;\; 0 \;\; 0 \;\; 0 \;\; 0 \;\; F_{Hy} \,] \end{aligned} \tag{44}$$

where τ_1 is the actuator input torque.

Since the actuator input torque τ_1 is unknown, Eq. (26) is used instead of Eq. (25), such that the constraint force can be calculated based on given τ_7, F_{Hx} and F_{Hy}, and then determine τ_1 using the constraint force λ. The corresponding Q_{ei} and Q_{ed} are

$$Q_{ei} = \tau_1 \tag{45}$$

and

$$Q_{ed} = [\;\; 0 \;\; \cdots \;\; 0 \;\; 0 \;\; 0 \;\; 0 \;\; \mp F_{Hy} \,] \tag{46}$$

According to Eq. (26), the constraint force under given generalised external force is

$$\lambda = C_{qd}^{-T} Q_{ed} \tag{47}$$

Following Section 3.5, Eq. (47) at the overlapped and non-overlapped configurations is solved separately, which yields analytical and numerical solutions, respectively.

3.6.1. Analytical solution of λ at overlapped configuration

At the overlapped configuration, Eq. (47) which is solved with $c_{qGx|DG}$ is excluded from C_{qd}. The dimension of C_{qd} is 9 × 9 hence can be inversed directly. The analytical solution of cable tension, which are the first four elements in the constraint force λ, is given by

$$\lambda_1 = \begin{bmatrix} -\frac{F_{Hy}L_{AO}(-1+r+v+rv)}{rR(1+v)} \\ -\frac{F_{Hy}vL_{AO}}{rR} \\ -\frac{F_{Hy}vL_{AO}}{rR} \\ -\frac{F_{Hy}L_{AO}(-1+r)}{rR} \end{bmatrix} \tag{48}$$

for the upward direction of motion, and

$$\lambda_2 = -\lambda_1 \tag{49}$$

for the downward direction of motion. In both λ, the first to fourth rows correspond to cable tension between P1 and P2, P3 and P4, P4 and P5, and P6 and P7, respectively.

In Eq. (48), since F_{Hy} is negative, r is greater than 1, and R and v are positive, all the elements are positive. As such, the cable forces within Loops PL, FB and PU are all tension. Similarly, in Eq. (49), since F_{Hy} is positive, the cable forces are all positive. Hence, the cable loops are in tension at the overlapped configuration in both directions of motion of the cable linkage.

3.6.2. Numerical solution of λ at non-overlapped configuration

At the non-overlapped configurations, the redundant constraints cannot be removed, as cable tension needs to be solved. The dimension of C_{qd} is 10 × 9 and cannot be inversed directly. QR decomposition is applied to obtain the numerical solution

$$C_{qd} = \begin{bmatrix} Q_1 & Q_2 \end{bmatrix} \begin{bmatrix} R_1 \\ 0 \end{bmatrix} \tag{50}$$

where θ_6 to θ_9, and L_{CG} in C_{qd} are represented in terms of θ_1 before QR decomposition is applied. Eq. (47) is written with Q_1 and R_1 as

$$\lambda = Q_1 R_1^{-T} Q_{ed} \tag{51}$$

The numerical solution of constraint force is plotted in Fig. 10, for full ROM of a sample cable linkage whose dimensions are listed in Table 5. The numerical solutions are identical for the upward and downward motions of the cable linkage.

In Fig. 10, P12, P34, P45 and P67 represent the cable tension in between Pulleys P1 and P2, P3 and P4, P4 and P5, and P6 and P7, respectively. The maximum cable tension is observed at the overlapped configuration. The magnitudes in Loops PL (P12), FB (P34 and P45) and PU (P67) are 119.1 N, 52.48 N, and 38.4 N, respectively, which agree with the analytical solutions. The cable tension P34 and P45 are identical, which also agrees with the analytical solution. The minimum tension are observed at both ends of ROM. The numerical solution indicates that the cable tension in all loops is positive within the full ROM.

3.6.3. Verification of cable tension and proof of Criterion 2

The numerical solution obtained from the constraint approach is verified with static rigid body simulation conducted using ANSYS Rigid Dynamics package, with a 2D model of the same sample cable linkage. The model used is shown in Fig. 11.

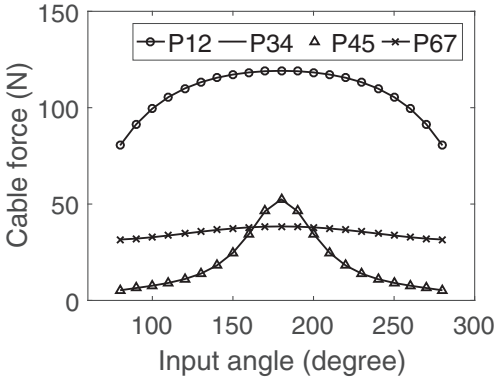

Fig. 10. Numerical solution of λ for sample cable linkage.

Table 5
Dimensions of sample cable linkage.

Parameters	Magnitude
L_{AO} (mm)	400
v	0.3
r	1.220
L_1 (mm)	120
L_2 (mm)	98.4
L_3 (mm)	72
R (mm)	15
F_{Hy} (N)	∓ 8

In the 2D model, links are used to mimic cable sections. The links are connected to pulleys with revolute joints, such that only tension and compression are allowed.

The cable tension in one side of the cable loop is obtained by summing the magnitudes of tensile and compressive of the two links which are connected to the same pulley. To justify the direction of cable force, the joint force at the link corresponding to the cable that is expected to be in tension must be tension as well. The external force F_{Hy} is simulated by a remote force applied at the tip of Link EH.

The cable tension obtained through simulation is compared with the calculated results in Figs. 12 and 13. The legends with "S" correspond to the simulation results.

The comparison indicates that the cable tension in Loops PL and PU, as well as the actuator input torque τ_1 obtained through the constraint approach is accurate. In Loop FB, exact solution is obtained at the overlapped configuration. The errors are relatively large towards two ends of the ROM, but the trend in the change in cable tension with respect to input angle is well captured. Therefore, the cable tension calculated from the constraint approach is verified, and it can be concluded that Criterion 2 for functioning of cable loops is proven.

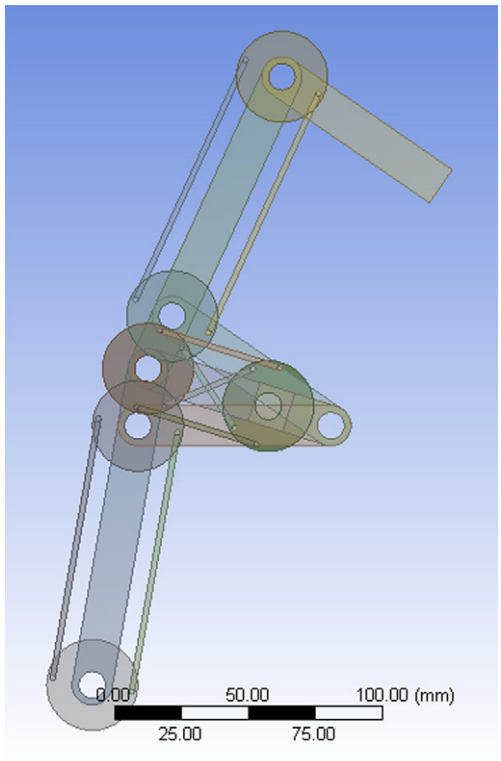

Fig. 11. 2D model in ANSYS.

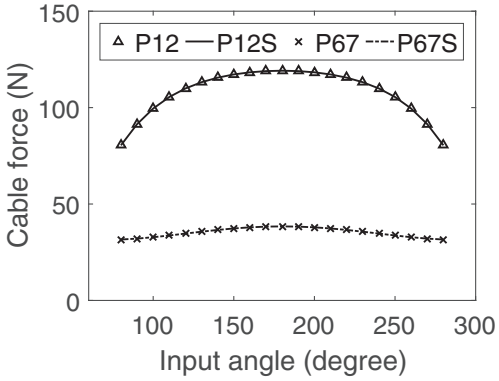

Fig. 12. Comparison of cable tension in Loops PL and PU.

4. Calculation on cable stiffness

The stiffness of the cable linkage is defined as the deformation of Point H under external load

$$k = \frac{F_{Hy}}{dy_H} = \frac{8\text{N}}{5\text{mm}} = 1.6\text{N/mm} \tag{52}$$

The stiffness of the cable must be sufficient to achieve the overall stiffness. Since cable tension and elongation change with respect to the movement of the linkage, the maximum value is determined as the minimum required cable stiffness

$$k = \max\left(\frac{\lambda_i}{dL_i}\right) \tag{53}$$

where k is the minimum required cable stiffness in the cable loop. λ_i and dL_i are the cable tension at different actuator input angle and its corresponding elongation, respectively.

Due to the assumption of inextensible cable, conventional definition of elongation, which is defined as deformation of cable, cannot be applied in the analysis. Here, the elongation is defined as the infinitesimal travel distance of cable with respect to infinitesimal displacement at Point H dy_H. The derivation of cable elongation is presented as follows.

The travel distance of cable is related length of cable wrapping on pulley and hence can be written in terms of generalised coordinates

$$dL = \text{function}\,(R,\quad \theta_{in},\quad \theta_q,\quad \theta_{out}) \tag{54}$$

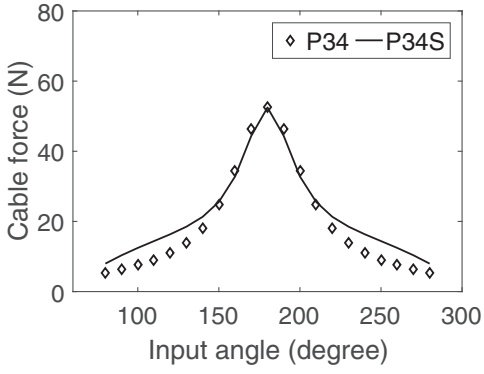

Fig. 13. Comparison of cable tension in Loop FB.

where the function is the suitable equation among Eqs. (30) to (33). θ angles are listed in Table 2 or 3. The mathematical expressions are (use P1, P3 and P6 for upward motion as examples)

$$\begin{aligned} dL_{PL} &= Rd\theta_1 \\ dL_{FB} &= Rd\theta_8 \\ dL_{PU} &= Rd\theta_6 \end{aligned} \tag{55}$$

where dL_{PL}, dL_{FB} and dL_{PU} are the infinitesimal cable travel in Loops PL, FB and PU, respectively. $d\theta_1$, $d\theta_8$ and $d\theta_6$ are the infinitesimal change in generalised coordinates.

Eq. (55) needs to be further related to dy_H using Eq. (24). Rearranging yields

$$dq_d = -C_{qd}^{-1} C_{qi} dq_i \tag{56}$$

where dq_d and dq_i are the infinitesimal change in dependent and independent generalised coordinates, respectively. dy_H, $d\theta_8$, and θ_6 are contained in dq_d, while $d\theta_1$ is dq_i. Eq. (56) writes $d\theta_1$ in terms of dy_H. All other dependent generalised coordinates are written in terms of $d\theta_1$ and hence related to dy_H.

Eq. (56) is solved numerically using QR decomposition as

$$dq_d = -R_1^{-1} Q_1^T C_{qi} dq_i \tag{57}$$

where Q_1 and R_1 are obtained from Eq. (50). Substituting Eq. (57) into Eq. (55) yields the infinitesimal travel distance of cable in the cable loops. Further substituting such infinitesimal travel distance of cable into Eq. (53) gives the minimum required cable stiffness corresponding to the overall system stiffness. The results are illustrated in Fig. 14.

The minimum required cable stiffness are 240.5 N/mm, 137.7 N/mm and 77.51 N/mm for Loops PL, FB and PU, respectively. In all three cable loops, the largest k are observed at the overlapped configuration. The pattern of change in k with respect to input angle in Fig. 14 is very similar to the pattern of change in tension with respect to input angle in Fig. 10, which means the cable tension is the dominating factor in stiffness.

5. Comparison on device footprint

For a 2-DOF RCM mechanism based on the cable linkage, the footprint is described through three approaches

1. The sweeping volume of linkage.
2. The space behind the input joint to permit the rotation of input link.
3. The volume of links.

In this section, the footprint of cable-linkage is compared to that of a PB-linkage through the above-mentioned approaches.

The comparison of footprint is conducted mathematically under a simplified surgical scenario, as shown in Figs. 15 and 16, for the cable linkage and PB-linkage, respectively. Five configurations of both RCM mechanisms are shown, which are the two extremes in ROM, centre and two mid-point configurations as presented in Figs. 3 and 4.

In the simplified surgical scenario, the incision port is Point O. The ROM to be achieved is symmetric around the ground axis. R_C is a coefficient less than one. It gives the radius of the circular region in terms of distance L_{AO}, where the links (except for the

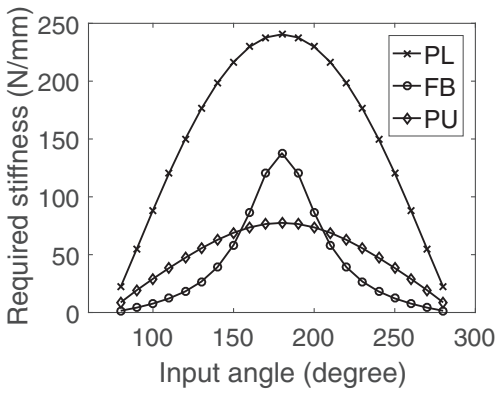

Fig. 14. Cable stiffness.

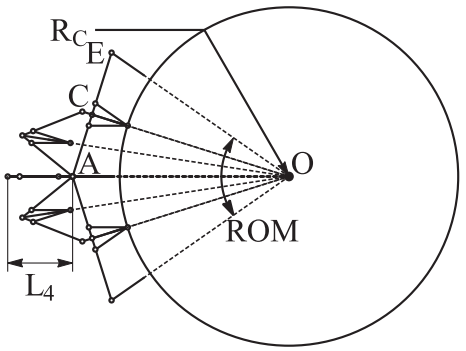

Fig. 15. Cable linkage in surgical scenario.

output link) of the RCM mechanisms are not allowed to enter such region. The region with R_C is set, such that more clearance near the incision port is left for the output links of multiple surgical arms and human surgeons to occupy.

L_{AO} is the same for both RCM mechanism. The ROM is changed from 30 to 120°. R_C is changed from 0.5 to 0.825. The dimensions and hence the footprints of the RCM mechanisms are calculated based on the given set of ROM and R_C.

For the cable linkage, the lengths of input and connector links (AC and CE) are determined from the ROM using Eq. (3). The lengths of BG and DG are calculated from Eq. (4), where r is assumed to be 1.22 and not changed in the simulation. For the PB-linkage, the length of input link AC is the same as the radius defined by R_C and L_{AO}, such that the output joint C is just on the edge of the circle. The length of connector link BC equals L_{AO}.

The results of the comparison are presented as the percentage difference of the footprint of cable linkage, over that of the PB-linkage, expressed as

$$\delta = \frac{f_{CL} - f_{PB}}{f_{PB}} \times 100\% \tag{58}$$

where f_{CL} and f_{PB} are the footprints of the cable linkage and PB-linkage, respectively.

5.1. Approach 1

In MIS applications, a planar RCM mechanism with smaller enclosed area is desired, such that the sweeping volume and the chance of collision between surgical arms are reduced.

In Approach 1, the footprint is described as the characteristic enclosed area. Such characteristic enclosed area is calculated by summing the four out of five configurations in Figs. 15 and 16, such that the change in enclosed area with respect to movement of linkage is taken into account. The overlapped configuration is not considered, as the enclosed area is zero. The mathematical expression is

$$f_1 = f_{top} + f_{mid-top} + f_{mid-bottom} + f_{bottom} \tag{59}$$

where f_1 is the characteristic enclosed area and the four remaining f terms are the enclosed area at four configurations, respectively. The enclosed area of the cable linkage and PB-linkage is defined by four-bar linkage ACEO and parallelogram ABCO in Figs. 15 and 16, respectively. The results are illustrated as a contour plot in Fig. 17.

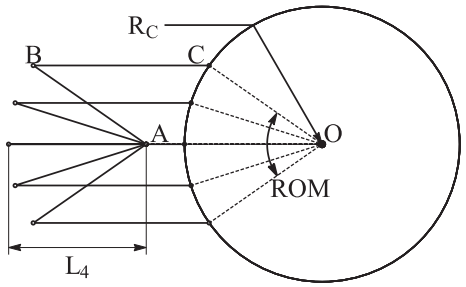

Fig. 16. PB-linkage in surgical scenario.

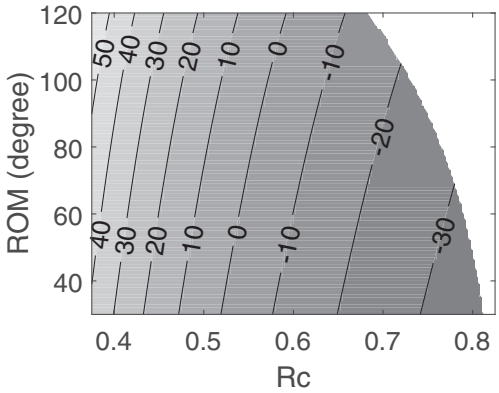

Fig. 17. Percentage difference in footprint - Approach 1.

The blank region at the top right corner of Fig. 17 is where the cable link fails to stay outside the radius with given R_C. The edge of such region corresponds to the configuration of the cable linkage, where Joint G is on the edge of the circle, as illustrated in Fig. 15.

The result reveals that the enclosed area of the cable linkage is smaller than that of the PB-linkage in about half of the design points (sets of ROM and R_C). The cable linkage has smaller enclosed area at large R_C (>0.5). The smallest enclosed area is achieved at the maximum R_C of 0.81, and the corresponding percentage difference is -35 %. Cable linkage has a relatively smaller enclosed area because its geometry is fully defined by the ROM (when r is given). In the contrast, the length of Links AB and CO and hence the footprint of the PB-linkage increase with R_C.

5.2. Approach 2

Both RCM linkage require additional clearance behind input joint A to allow the movement of linkage. As such, the region needs to be kept clear during the operation. A large region will increase the space needed to maneuver the linkage. In addition, a large region requires a larger base to hold the RCM mechanism, thus increases the overall dimension of the robotic manipulator.

The footprint in terms of the aforementioned region is represented by the sweeping L_4 in Figs. 18 and 19 around Joint A and behind Joint A. For cable linkage, L_4 equals L_{AC}. Link AC is behind Joint A when actuator input angle is within $\pi/2$ to $3\pi/2$. For PB-linkage, L_4 equals the length Link AB and thus the radius of circle. Link AB sweeps behind Joint A in the full ROM. The mathematical expressions are

$$f_{CL2} = \frac{1}{2}\pi L_4^2 \qquad (60)$$
$$f_{PB2} = \frac{ROM}{2\pi}\pi L_4^2$$

The results are illustrated as a contour plot in Fig. 20.

The result shows that the footprint (Approach 2) of the cable linkage is smaller than that of the PB-linkage in more than half of the design points. The maximum reduction in footprint is 83% at ROM of 30° and R_C equals 0.8. The footprint of the cable linkage is smaller in the cases where ROM is small and/or R_C is large. On the other hand, since the dimension of the cable linkage is defined by the ROM, the footprint is large at large ROM and/or small R_C.

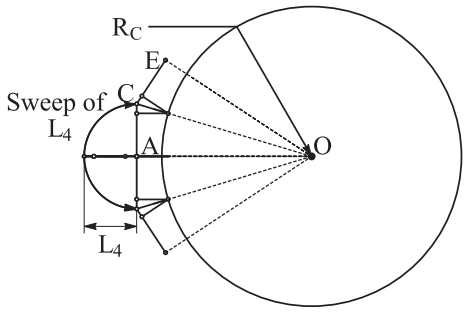

Fig. 18. Cable linkage in surgical scenario.

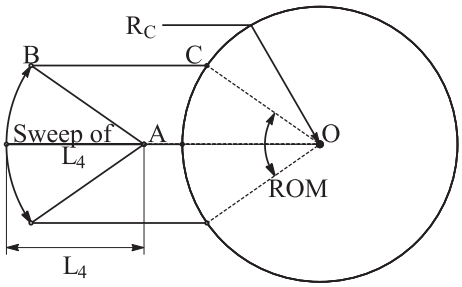

Fig. 19. PB-linkage in surgical scenario.

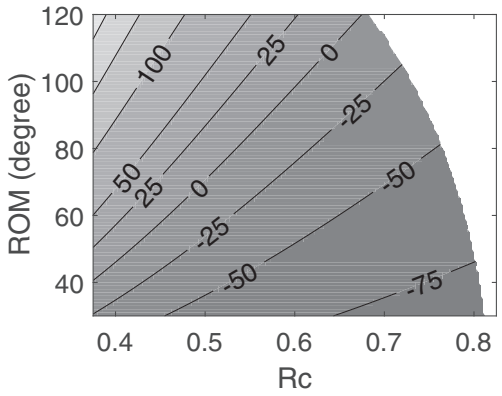

Fig. 20. Percentage difference in footprint - Approach 2.

5.3. Approach 3

There are cases in MIS applications where a surgical manipulator stays stationary while the other robotic arms or human surgeons are conducting manipulations. Therefore, the footprint in terms of the volume taken by the stationary links themselves must be taken into account.

Since the volume of the links is proportional to the length of links, the sum of lengths of links is used as the measurement of footprint in Approach 3. For cable linkage, the links involved are Links AC, CE, BG and DG. Diagonal link CG is not considered as it is enclosed by BG and DG. For PB-linkage, the links involved are Links AB and BC. The mathematical expressions are

$$f_{CL3} = L_{AC} + L_{BG} + L_{DG} + L_{CE} \tag{61}$$
$$f_{PB3} = L_{AB} + L_{BC}$$

The results are illustrated as a contour plot in Fig. 21.

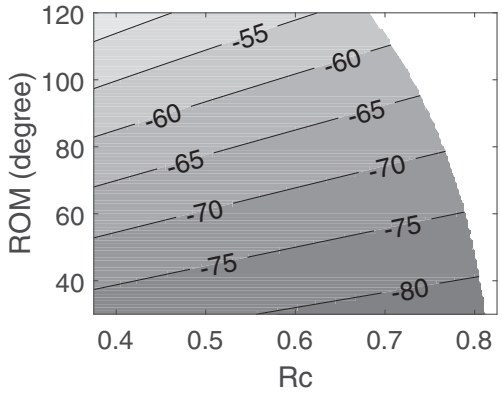

Fig. 21. Percentage difference in footprint - Approach 3.

The figure shows that the footprint (Approach 3) is smaller than that of the PB-linkage in all the achievable design points. The percentage reduction in footprint varies between −50% and −80 %, which is significant. Again, the cause of the difference is the fact that the footprints of two RCM mechanisms are dependent on ROM and R_C, respectively, while irrelevant to the other.

The comparison in footprint through three approach shows that the cable linkage has a smaller sweeping volume and requires less space behind the input joint in more than half of the design points. In addition, the overall lengths of the links are shorter in all design points, resulting in smaller and lighter linkage. Therefore it can be concluded that the cable linkage has advantages over the PB-linkage in terms of footprint in MIS applications. The scenario that suits the cable link best is where the required ROM is relatively small while the RCM mechanism has to be kept faraway from the incision port.

6. Prototype of cable linkage

A passive concept-proving prototype of the cable linkage is built. The dimensions of the linkage are given in Table 5. The ROM is 69°, which satisfies the requirement of 60° ROM in most of the abdominal MIS applications [16]. The additional 9° are added such that v is 0.3 and L_1 is an integer. r is selected to be 1.22 to minimise rounding of L_2 and L_3. The selection of v and r helps reducing machining error and thus the potential positioning error of the remote centre. Note that due to the limit on the available cable, the minimum required stiffness presented in Fig. 14 is not applied on the cable in Loop FB.

The mechanical constraint of a cable loop can be achieve identically through end-less tendon drive or open-ended tendon drive, as classified in [25]. End-less tendon drive is literally closed-loop cable. It is structurally simpler and can theoretically be fully controlled by less actuators comparing to the open-ended tendon. On the other hand, open-ended tendon drive, which actively controls a pulley with two antagonistic tendons that are connected to their own actuators, respectively, yields zero or small backlash in the expanse of complexity. As the prototype is built for proof of concept, closed-loop cable is implemented in the prototype. To minimise the backlash, timing belt is used and the pre-tension is applied.

The CAD model of the cable linkage, showing two limits and the centre of the ROM, is illustrated in Fig. 22. The centre and lower limit configurations are combined in the figure by photoshop hence are semi-transparent. The sphere at the bottom right corner of the figure indicates the RC. The design of output link is arbitrary and yet to be optimised for specific MIS applications. The output ROM is 105 to 175° from the positive x-direction. The belts and cable sections are not shown.

A side view of the prototype is illustrated in Fig. 23. In the prototype, the widths of Links AC and CE are 16 mm. The radius of pulleys in Loops PL and PU is reduced to 12 mm due to the available pulley size. It can be observed from the figure that the area enclosed by Loops PL and PU is not significantly larger than the sizes of Links AC and CE, despite the outstanding tensioners located in the middle of the links. In addition, the pulleys in Loop FB are mostly enclosed by Links BG and DG in the side view, thus do not cause significant increase in the size of mechanism.

Top views of the prototype are illustrated in Figs. 24 and 25. Fig. 24 annotates the links and Loops PL and PU. In both loops, timing belts are used to minimise backlash. It also eliminates the chance of slip of cable on pulleys in Loops PL and PU, where the consequence of such cable slip is the lost of RCM function. To increase the rigidity of the mechanism, a duplicated pair of Links AC and AF is introduced. Both links are located above Links CE, P6 and P7 in Fig. 24.

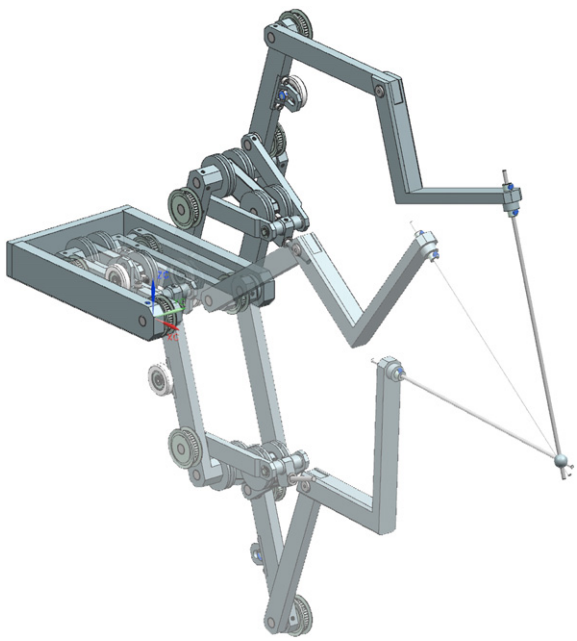

Fig. 22. CAD model of cable linkage.

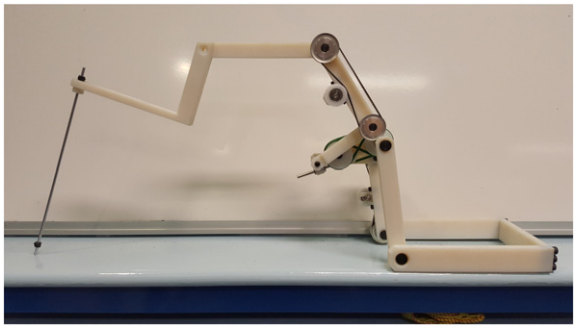

Fig. 23. Right side view of prototype.

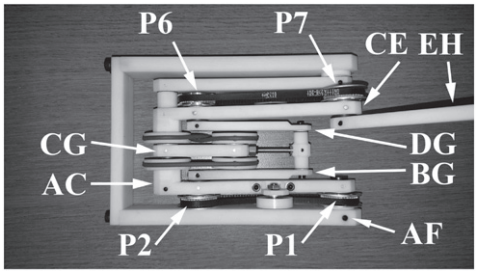

Fig. 24. Top view of prototype 1.

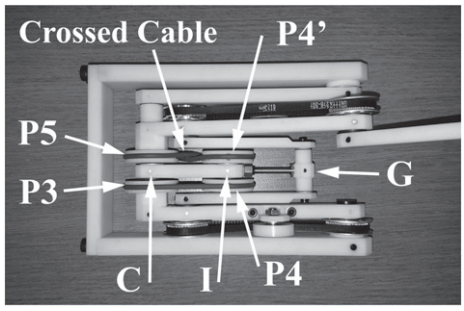

Fig. 25. Top view of prototype 2.

Fig. 25 annotates Loop FB. In this prototype, Loop FB is achieved by using two cable loops, one between P3 and P4 and the other between P4 and P5. Two pulleys, P4 and P4′ are rigidly connected to each other and mounted at Joint I. P4 is connected to P3, and P4′ is connected to P5 with crossed cable. Pulleys P3 and P5 are rigidly connected to Links AC and CE, respectively, by 3D-printing the pulley and the link as one part. To enable the crossed configuration of cable between P4′ and P5, a round belt is used.

The presence of tension in the correct sides of cable loops is vital for verifying the design concept. On the other hand, the exact magnitude of tension is of less importance, as it is primarily used as a prototyping guideline. The sign of cable tension can be readily observed through higher transverse cable stiffness on the driving side of a cable loop than that on the driven side. By manually applying force at the output link and comparing the cable stiffness, it is found that the presence of tension within the full range of motion is consistent with Figs. 5 and 6, as well as the outcomes in Section 3 . Apart from that, the prototype is manipulated to the centre configuration, where loads are applied manually in the attempt to force the prototype into the undesired configuration. Jamming of linkage is observed, thus verifies that the linkage can only turn into the desired configuration.

7. Conclusion

This paper introduces a cable linkage with RCM. The design of the cable linkage is presented, and proof on RCM function is conducted mathematically.

The tension in all cable sections is determined by means of a constraint approach. The analytical solution at the overlapped configuration is derived. The numerical solution at non-overlapped configurations are obtained through QR decomposition. The tensions are positive within the full working range, validating the function of the linkage.

The cable tension calculated is verified through finite element simulation. The constraint approach yields exact solution of cable tension in Loops PL and PU within full ROM, and in Loop FB at overlapped configuration. The error in Loop FB at non-overlapped configurations is small.

The constraint approach is further used to determine the minimum required cable stiffness, corresponding to a given overall system stiffness at the output link. Both the tension and infinitesimal displacement of cable are derived from the constraint approach and solved with QR decomposition.

Quantitative comparison between the footprints of the cable linkage and PB-linkage is conducted in a simplified surgical scenario. The footprint is described in three approaches. In two of the approaches, the cable linkage yields smaller footprint in half of the design points. In the last one the cable linkage achieves 50% to 80% reduction in footprint.

A prototype is constructed for proof of concept. Closed-loop cable is used to simplify the architecture. Timing belts are used in Loops PL and PU to prevent slip of cable on pulley. Loop FB is further divided into two loops, in between P3 and P4, and P4′ and P5, respectively. Round belt is implemented between P4′ and P5 to enable crossed cable configuration. The correct presence of tension within full range of motion, as calculated in Section 3, is validated. The prototype is also proved to be prevented from turning into the undesired configuration.

Appendix A. Supplementary data

Supplementary data to this article can be found online at http://dx.doi.org/10.1016/j.mechmachtheory.2016.07.023.

References

[1] C.-H. Kuo, J.S. Dai, P. Dasgupta, Kinematic design considerations for minimally invasive surgical robots: an overview, Int. J. Med. Rob. Comput. Assisted Surg. 8 (2) (2012) 127–145.
[2] R.H. Taylor, D. Stoianovici, Medical robotics in computer-integrated surgery, IEEE Trans. Robot. Autom. 19 (2003) 765–781.
[3] C.H. Kuo, J.S. Dai, Robotics for minimally invasive surgery: a historical review from the perspective of kinematics, Proc. History of Machines and Mechanisms, Tainan, Taiwan, 2008, pp. 337–354.
[4] G. Zong, X. Pei, Classification and type synthesis of 1-DOF remote center of motion mechanisms, Mech. Mach. Theory 43 (2008) 1585–1595.
[5] C. Chen, M. Pamieta, Novel linkage with remote center of motion, Proc. 3rd IFToMM International Symposium on Robotics and Mechatronics, Vol. 2,Singapore, 2013, pp. 139–147.
[6] M. Ghodoussi, S.E. Butner, Y. Wang, Robotic surgery - the transatlantic case, Proc. IEEE International Conference on Robotics and Automation (ICRA), vol. 2, 2002, pp. 1882–1888.
[7] A. Guerrouad, P. Vidal, SMOS: stereotaxical microtelemanipulator for ocular surgery, Proc. Annual International Conference of the IEEE Engineering in Medicine and Biology Society, Vol. 3,Seattle, USA, 1989, pp. 879–880.
[8] E. Hempel, H. Fischer, L. Gumb, T. Höhn, H. Krause, U. Voges, H. Breitwieser, B. Gutmann, J. Durke, M. Bock, A. Melzer, An MRI-compatible surgical robot for precise radiological interventions, Comput. Aided Surg. 8 (2003) 180–191.
[9] A.J. Madhani, G. Niemeyer, J.K. Salisbury, The black falcon: a teleoperated surgical instrument for minimally invasive surgery, Proc. IEEE/RSJ International Conference on Intelligent Robots and Systems, vol. 2,Victoria, British Columbia, 1998, pp. 936–944.
[10] R.H. Taylor, J. Funda, D.D. Crossman, J.K. Karidis, D.A. LaRose, Remote Center-of-Motion Robot for Surgery, 1995.
[11] S.J. Blumenkranz, D.J. Rosa, Manipulator for Positioning Linkage for Robotics Surgery, 1995.
[12] M. Feng, Y. Fu, B. Pan, C. Liu, Development of a medical robot system for minimally invasive surgery, Int. J. Med. Rob. Comput. Assisted Surg. 8 (2012) 85–96.
[13] K. Kim, H. Song, S. Park, J. Lee, Y. Yoon, Design and evaluation of a teleoperated surgical manipulator with an additional degree of freedom for laparoscopic surgery, Adv. Robot. 24 (2010) 1697–1718.
[14] W.H. Zhu, S.E. Salcudean, S. Bachmann, P. Abolmaesumi, Motion/Force/Image control of a diagnostic ultrasound robot, Proc. IEEE International Conference on Robotics and Automation (ICRA), vol.2, San Francisco, USA, 2000, pp. 1580–1585.
[15] D. Stoianovici, L.L. Whitcomb, D. Mazilu, R.H. Taylor, R.L. Kavoussi, Remote Center of Motion Robotic System and Method, 2004.
[16] M.J.H. Lum, D.C.W. Friedman, G.S.H. King, K. Fodero, R. Leuschke, B. Kannaford, J. Rosen, M.N. Sinanan, The REVAN: design and validation of a telesurgery system, Int. J. Robot. Res. 28 (2009) 1183–1197.
[17] G. Bai, D. Li, S. Wei, Q. Liao, Kinematics and synthesis of a type of mechanisms with multiple remote centers of motion, Proc. IME. C. J. Mech. Eng. Sci. 228 (18) (2014) 3430–3440.
[18] R.R. Solomon, T. Cooper, Multi-ply Strap Driver Trains for Robotic Arms, 2007.
[19] G. Haber, M.A. White, R. Autorino, R.F. Escobar, M.D. Kroh, S. Chalikonda, R. Khanna, S. Forest, B. Yang, F. Altunrenda, R.J. Stein, J.H. Kaouk, Novel robotic da Vinci instruments for laparoendoscopic single-site surgery, Urology 76 (2010) 1279–1282.
[20] H. Long, Y. Yang, X. Jingjing, S. Peng, Type synthesis of 1R1T remote center of motion mechanisms based on pantograph mechanisms, J. Mech. Des. 138 (1) (2016) 014501.
[21] J. Li, Y. Xing, K. Liang, S. Wang, Kinematic design of a novel spatial remote center-of-motion mechanism for minimally invasive surgical robot, J. Med. Devices 9 (1) (2015) 011003.
[22] M. Hadavand, A. Mirbagheri, S. Behzadipour, F. Farahmand, A novel remote center of motion mechanism for the force-reflective master robot of haptic tele-surgery systems, Int. J. Med. Rob. Comput. Assisted Surg. 10 (2) (2014) 129–139.
[23] R.H. Taylor, D. Stoianovici, Is smaller workspace a limitation for robot performance in laparoscopy? J. Urol. 179 (2008) 1138–1143.
[24] D.W. Hong, R.J. Cipra, A method for representing the configuration and analyzing the motion of complex cable-pulley systems, J. Mech. Des. 125 (2) (2003) 332–341.

[25] L.-W. Tsai, Design of tendon-driven manipulators, J. Vib. Acoust. 117 (B) (1995) 80–86.
[26] X. Tang, An overview of the development for cable-driven parallel manipulator, Adv. Mech. Eng. 6 (2014) 823028.
[27] L.-W. Tsai, J.-J. Lee, Kinematic analysis of tendon-driven robotic mechanisms using graph theory, J. Mech. Transm. Autom. Des. 111 (1) (1989) 59–65.
[28] D. Lau, D. Oetomo, S.K. Halgamuge, Generalized modeling of multilink cable-driven manipulators with arbitrary routing using the cable-routing matrix, IEEE Trans. Robot. 29 (5) (2013) 1102–1113.
[29] C. Chen, Power analysis of epicyclic transmissions based on constraints, J. Mech. Robot. 4 (2012)
[30] A.A. Shabana, Computational Dynamics, Wiley, Chichester, UK, 2010.